Thin Solid Films 519 (2010) 331–336

Contents lists available at ScienceDirect

Thin Solid Films

journal homepage: www.elsevier.com/locate/tsf

Fracture behavior of nano-layered coatings under tension

Herzl Chai [a,*], Daniel Josell [b]

[a] School of Mechanical Engineering, Faculty of Engineering, Tel-Aviv University, Tel-Aviv, Israel
[b] Metallurgy Division, MSEL, National Institute of Standards and Technology, Gaithersburg, MD 20899, United States

ARTICLE INFO

Article history:
Received 18 February 2010
Received in revised form 16 July 2010
Accepted 19 July 2010
Available online 29 July 2010

Keywords:
Thin films
Si/Ag
Multilayers
Fragmentation
Tunnel cracks
Fracture toughness

ABSTRACT

The fracture of brittle/ductile multilayers composed of equal thicknesses of Si and Ag layers evaporated on a thick substrate is studied with the aid of a four-point bending apparatus. The system variables include individual layer thickness (2.5 to 30 nm), total film thickness (0.5 to 3.5 μm) and substrate material (polycarbonate, aluminum alloy and hard steel). The fracture is characterized by transverse cracks that proliferate with load. The crack initiation strain ε_i is virtually independent of total film thickness and substrate material while increasing with decreasing layer thickness h, to a good approximation as $\varepsilon_i \sim 1/h^{1/2}$. At higher strains, film debonding and buckling are evident.

The fracture conditions are determined with the aid of a 2D finite element analysis incorporating the inelastic response of the interlayer. A fracture scenario consisting of tunnel cracking in the brittle layers followed by cracking in the interlayers is shown to be capable of predicting the observed increase in crack initiation strain with decreasing layer thickness. To realize this benefit the interlayer must be compliant and tough to force tunnel cracking in the brittle layers. The explicit relation for the crack initiation strain obtained from the analysis can be used to assess fracture toughness and improve damage tolerance in nanoscale layered structures.

1. Introduction

It is well recognized that the mechanical properties of thin films may be vastly enhanced using multiple nanometer-scale layers (multilayers). Tensile tests on free-standing multilayers composed of alternating nano-size layers of various constituents such as Al/Cu [1], Al/Ti [2], Ag/Cu [3] and Ni/Cu [4] show an increase in yield strength with decreasing individual layer thickness. Similar improvement is also reported for hardness [5,6]. Such trends are generally attributed to size effects and changes in grain structures and density and movement of dislocations affected by the multilayer interfaces. Unlike the constitutive response, fracture studies on ultra-thin multilayers are scarce. It is this issue that is of main interest here.

Understanding the fracture behavior of multilayer films is complicated by a wealth of material and geometric variables, the effects of exterior factors such as surface flaws and thermal stresses, and a lack of direct information on the interior fracture process. Most fracture works on multilayers rely on indentation techniques that, while straightforward to apply, treat the multilayer as a homogeneous medium when evaluating fracture toughness (e.g., [7,8]). A more suitable approach is afforded by film/substrate configurations loaded in direct tension or bending, for which a state of uniform tension in the film prevails. Ref. [9] employed a simple-support bending test to study crack initiation in nano-scale Cu/Ni multilayers on flexible substrates. However, again the multilayer was treated as a homogeneous film in calculating fracture toughness. Fracture analyses considering the layered nature of the structure are generally limited to tri-layer laminates [10]. In this work the fracture behavior of full-fledged, nanometer-scale multilayers was studied experimentally and analytically.

As pictured schematically in Fig. 1a, our specimen consists of alternating, equal-thickness brittle silicon (Si) and ductile silver (Ag) layers evaporated on thick substrates. The layer thickness h and total film thickness t varied from 2.5 to 30 nm and 0.5 to 3.5 μm, respectively. Polycarbonate, aluminum alloy and hard steel substrates were used. As shown in Fig. 1b the specimens were loaded in a four-point bending fixture that provides essentially a uniform state of tension in the film. The evolution of damage in the film with load was recorded in real-time. The experiments are complemented by a 2D finite element analysis (FEA) aimed at quantifying the dependence of measured crack initiation strain ε_i on material and geometric variables. The analysis, which takes into account the internal film architecture and the inelastic response of the interlayer, considers steady-state tunnel cracking in the hard layers and edge cracking in the ductile layers as the main fracture modes. The experimental apparatus and test results are reported in Sections 2 and 3, respectively. The fracture mechanics analysis is presented in Section 4. Section 5 discusses the results in the context of more general systems.

2. Experimental details

The multilayers were deposited on 3 mm square cross-section, beam-shaped substrates by a three-source electron beam evaporator using

* Corresponding author.
E-mail address: herzl@eng.tau.ac.il (H. Chai).

0040-6090/$ – see front matter © 2010 Elsevier B.V. All rights reserved.
doi:10.1016/j.tsf.2010.07.086

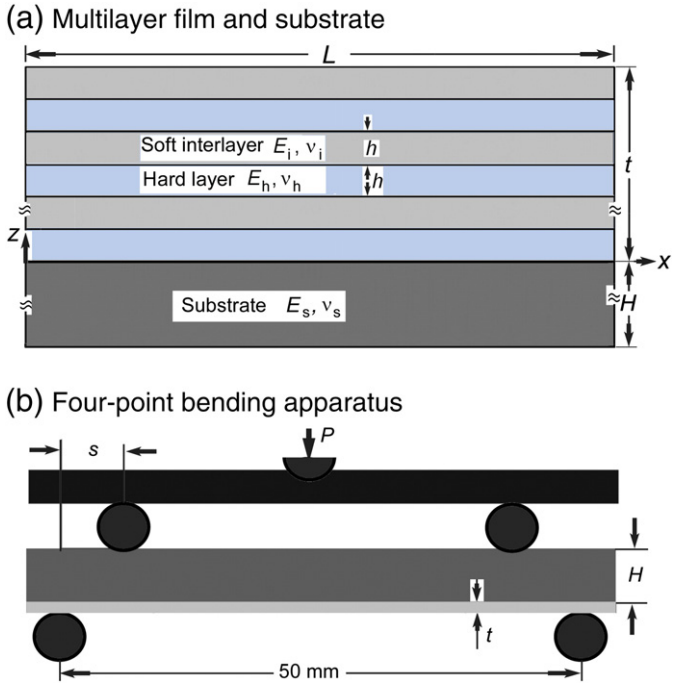

Fig. 1. Schematics of sputtered-deposited multilayer film on substrate (a) and four-point bending specimen used for the fracture tests (b). The film, of total thickness t, consists of alternating brittle/ductile Si/Ag layers of equal thickness h. The substrate, of thickness H, is polycarbonate, 7075-T6 aluminum alloy or AISI O1 tool steel.

charges of silver (Ag) and silicon (Si) source materials (both > 99.99 mass % purity). Polycarbonate, 7075-T6 aluminum alloy and AISI O1 tool steel were used as substrates. The latter was preheated to 785 °C and quenched in a bath of oil for 12 min before it was tempered at 200 °C for 2 h. Table 1 lists some relevant material data from the literature. The surfaces of the metal substrates were polished with 1 μm suspended diamond particles and cleaned in an ultrasonic bath of acetone. To further enhance bonding between films and substrates, the latter were cleaned in-situ by argon ion sputtering just prior to evaporation. To reduce thermal stresses, the specimen holder was cooled by running water. Deposition rate and thickness monitors were used to control source shutters that alternately exposed the substrates to the sources. The thicknesses of the Si and Ag layers are equal within each specimen. As shown in Fig. 1a, the thicknesses of individual layers, film and substrate are denoted as h, t and H, in that order. Films with dimensions $h = 2.5$, 5, 10, 30 nm and $t = 0.5$, 1, 1.7, 2.6, 3.5 μm were fabricated. All specimens with a particular layer thickness were fabricated simultaneously; the different total film thicknesses were obtained by covering some substrates with a shutter during the deposition process.

Fracture tests were conducted using the four-point bending apparatus shown in Fig. 1b. The width and thickness of the beams are $b = 3$ mm and $H = 3$ mm while the distance between upper and lower loading pins, s, is 7.5 mm. Loading was applied by a standard loading frame operated in a stroke-controlled mode. The crosshead speed was adjusted such that film cracking occurred within 2 to 3 min. The evolution of surface cracks with load was monitored with the aid of a video camera fitted with a zoom lens. The load and other test variables were superimposed on each image to aid in the subsequent data analysis. The macroscopic tensile strain ε generated in the multilayer due to force P was calculated using standard beam theory that incorporates the inelastic response of the substrate. Within the strain range of interest here (ε < 1.5%) the stress-strain response of polycarbonate is essentially linear while that of the metals is approximated by a bilinear relation of the form

$$\sigma = E_s \varepsilon, \varepsilon < \varepsilon_{Ys} \tag{1a}$$

$$\sigma = E_s \varepsilon_{Ys}(1+\gamma\varepsilon/\varepsilon_{Ys}-\gamma), \varepsilon > \varepsilon_{Ys}, \tag{1b}$$

where E_s and ε_{Ys} are the Young's modulus and effective yield strain of the substrate and γ a coefficient in the range 0 to 1 that quantifies the amount of plasticity. Literature data ([11,12]) indicate that the pair (ε_{Ys}, γ) can be reasonably approximated as (0.77%, 0.33) and (0.63%, 0.24) for the hard steel and aluminum alloy, respectively. Ignoring the load carried within the film itself, a valid assumption because $t/H \ll 1$, the beam analysis shows that the tensile strain in the film is governed by the following cubic equation

$$2\gamma(\varepsilon/\varepsilon_{Ys})^3 + [3(1-\gamma) - 2\varepsilon_L/\varepsilon_{Ys}](\varepsilon/\varepsilon_{Ys})^2 = 1-\gamma, \varepsilon/\varepsilon_{Ys} > 1, \tag{2}$$

where $\varepsilon_L \equiv 3Ps/bEH^2$ is a reference strain corresponding to the limit case of linearly-elastic film and substrate (for which $\gamma = 1$). This equation was solved numerically, yielding a single real root over the range of input parameters of interest here.

While we have not directly measured the stress arising in the film from either thermal cycling during deposition or the deposition process itself, such a stress is believed to be very small. Because of the high thermal conductivity of the aluminum and steel substrates the temperature rise during deposition for these samples likely did not exceed a few °C. With the mismatch in thermal coefficient of expansion between Si and aluminum being about $20/10^6$ per 1 °C (Table 1), for a 10 °C temperature variation the thermal mismatch strain in the Si layers amounts to 0.02%. For the steel substrate the thermal mismatch strain would be about half that much. In the case of polycarbonate the thermal coefficient is about three times that for aluminum. However, relaxation of the polymer during cooling might be expected to reduce the thermal mismatch strain. (As will be seen later, further support for the relative insignificance of deposition strain is the absence of clear variation of the fracture data with substrate material.) Because thermal mismatch strains are small compared with the mechanical strain of interest here, in the following we neglect the initial strain and consider only the mechanical strain ε.

Table 1
Material parameters in this study[a].

Material	Young's modulus E [GPa]	Poisson's ratio ν	Coefficient of thermal expansion [μm/m °C]
7075-T6 al. alloy	70	0.35	23
AISI O1 steel	210	0.29	12
Polycarbonate	2.35	0.35	67
Si	130	0.28	2.6
Ag	63	0.34	18.9

[a] The elastic constants for aluminum, steel, polycarbonate and Ag are from Ref. [12], [11], [20] and [3], in that order. The rest of the data are taken from Wikipedia.

3. Test results

Fig. 2 shows a planview image of the fracture morphology for a 2.6 μm thick, 260-layer ($h = 10$ nm) film strained to ε = 0.55%. The damage is characterized by line cracks extending normal to the load axis that typically grew unstably from the specimen edges or from rough spots on the film surface. With increasing strain numerous debond or delamination regions developed from rough spots and grew along and normal to the crack line. Some of the delaminated segments tended to buckle, as evident by numerous dark strips in the print. Such buckling, likely due to a lateral contraction of the film relative to the substrate, was also encountered in tensile testing of ultra thin aluminum films on flexible substrates [13] and Al/SiC multilayers [14]. While the majority of buckled regions are fairly square, some elongated buckles are also apparent. The video records showed that the latter is due to a linkage of adjacent buckled regions. The behavior described above is common to all the specimens tested,

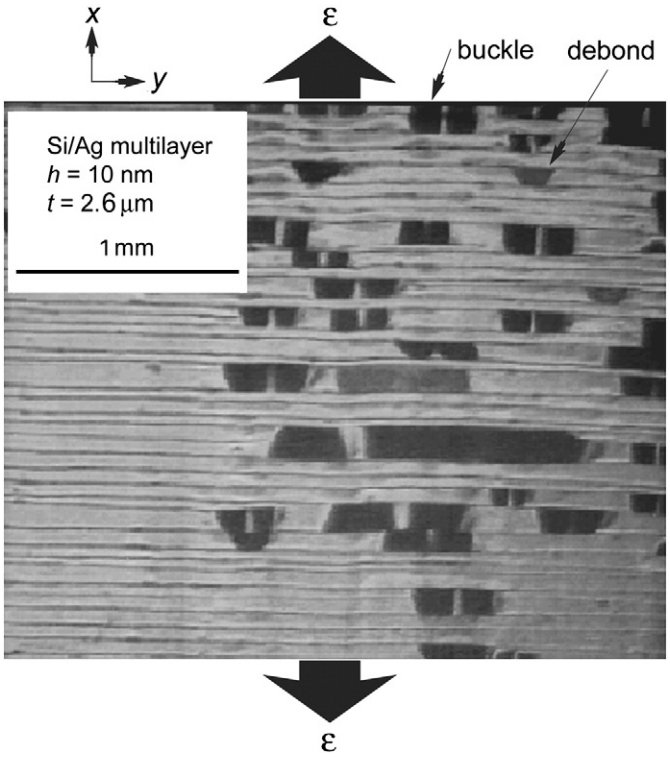

Fig. 2. Fracture morphology for Si/Ag multilayer on aluminum alloy substrate at tensile strain $\varepsilon = 0.55\%$. The fracture is characterized by line cracks running normal to the strain axis as well as by delamination and buckling. The cracks generally initiate from flaws at the edges or surface of the film.

albeit films with thicker individual layers exhibited larger and more intense delamination damage. In fact, in the case of the 30 nm layers entire strips of the films delaminated from the substrate as soon as a transverse crack formed. The presence of buckled segments indicates that the line cracks do penetrate the ductile layers.

Fig. 3 plots the number of cracks per 1 mm length along the beam or tensile direction vs. applied strain for the indicated specimens. The area observed for the measurements spans the entire beam width (3 mm) and a similar length along the beam direction. The data exhibit a well-defined strain for initial cracking that is followed by a moderating rate of increase in crack density that reflects a stress shielding effect [15]. Notwithstanding the scatter, there is a significant dependence on layer thickness h with no obvious dependence on total

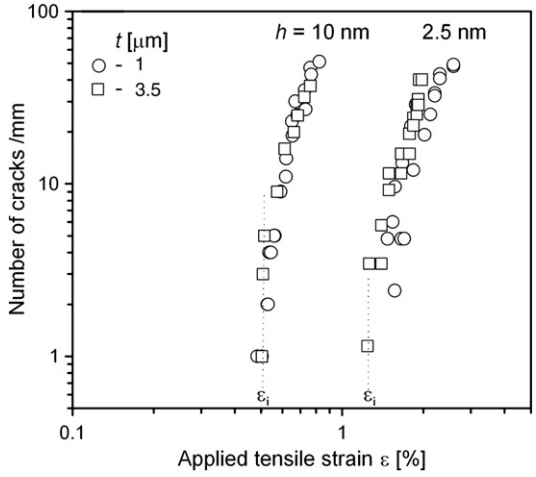

Fig. 3. Number of cracks per 1 mm length vs. applied strain for Si/Ag multilayer on aluminum alloy substrate, for configurations specified.

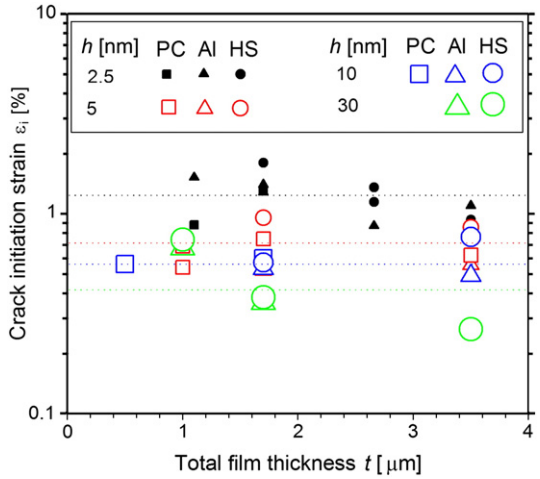

Fig. 4. Crack initiation strain vs. total film thickness for all Si/Ag multilayer specimens tested. The dotted lines are average values for each layer thickness h.

film thickness t. Fig. 4 summarizes the crack initiation strain ε_i vs. film thickness t for all the specimens tested. With the possible exception of specimens with the thickest layer ($h = 30$ nm), the crack initiation strain ε_i clearly increases with decreasing layer thickness but shows no systematic dependence on film thickness or substrate materials. Accordingly, we shall assume that ε_i is independent of total film thickness. The data in Fig. 4 are presented alternatively in Fig. 5 as crack initiation strain vs. layer thickness h, with different symbols denoting different substrate materials. The data points represent the mean values and standard deviations derived from the data for all film thicknesses. The crack initiation strain increases with decreasing layer thickness, to a good approximation as an inverse square-root $\varepsilon_i \sim 1/h^{1/2}$ (solid line). No significant dependence on substrate material is apparent.

4. Fracture mechanics

Of prime interest here is to quantify of the dependence of crack initiation strain on layer thickness seen in Fig. 5. Given from Figs. 3 to 5 that it is the internal multilayer architecture rather than total film thickness or substrate type that controls the fracture process, and noting the ability of the crack to penetrate the layered structure discussed earlier, we explored a number of fracture scenarios that have the potential to predict the experimental trend above. Fig. 6 details the fracture sequence adopted, where b is the specimen width and l and d

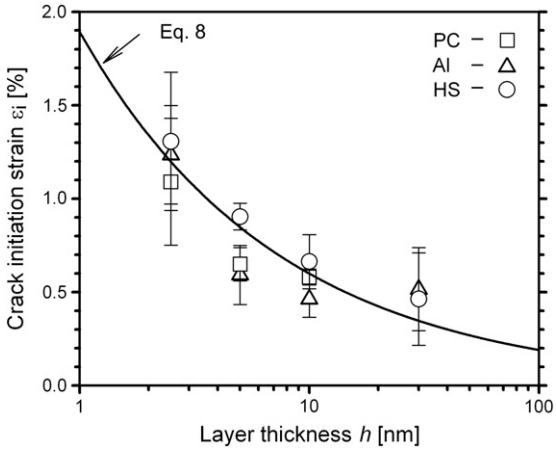

Fig. 5. Summary of crack initiation strain vs. layer thickness for Si/Ag multilayers. Symbols are experimental data, solid line is the model prediction. The data for each layer thickness and substrate material are represented by mean and standard deviation derived from the results from all total film thicknesses studied.

are the dimensions of an assumed pre-existing flaw at the specimen edge, shown as a gray shade in Fig. 6a. It is assumed that dimension d is much greater than the layer thickness, i.e., $d/h >> 1$. (In fact, d may be as large as the film thickness t.) Because of the low toughness of the hard layers it is reasonable to expect that the tunnel cracking mode (Fig. 6b) is the first to occur. Because $d/h >> 1$, the fracture would be collaborative so that all cracks grow spontaneously under the same boundary conditions. This is followed by a complete fracture in the strip $b \times d$, which is accomplished by *edge cracking* in the interlayers (Fig. 6c). We assume that this event signals a complete transverse fracture in the film.

A prime ingredient in our fracture analysis is the stress-strain response of the constituents. For the Si layers a linearly elastic behavior was assumed. We are unaware of a full stress-strain curve in the nanometer thickness regime for the ductile Ag so its response could only be inferred. The tensile testing of free-standing multilayer samples noted in the introduction suffers from premature failure due to stress concentration and necking. More recent tests employing advanced sample fabrication technology and nano-loading capabilities have circumvented this difficulty, extending the stress-strain response in some nano-size multilayers deep into the post-yield regime [16,17]. The results show that the response can be roughly approximated as elastic-perfectly plastic, which we assume to be the case for our Ag interlayers. Hence

$$\sigma = E_i \varepsilon, \varepsilon < \varepsilon_{Yi} \tag{3a}$$

$$\sigma = \sigma_{Yi}, \varepsilon > \varepsilon_{Yi}, \tag{3b}$$

where ε_{Yi}, σ_{Yi} and E_i are the yield strain, yield stress and Young's modulus of the interlayers.

The energy release rate (ERR) G for each of the two fracture modes detailed in Fig. 6 was calculated with the aid of a commercial FEM code (Ansys, Inc.; Information on product names and suppliers in this paper is provided for completeness of description and does not constitute endorsement by NIST). Plane-stress conditions were assumed so that small variations due to misfit in Poisson's ratios are ignored. As is generally the case when modeling the post-yield behavior of metals, the interlayer was assumed to obey von Mise's flow rule with incremental plasticity.

4.1. Tunnel cracking (Fig. 6b)

It is advantageous to discuss first the related case of channel cracking in a linearly elastic bilayer composed of a thin film on a thick substrate that is subjected to tensile strain ε normal to the crack plane. The essential features of this problem were captured by Nakamura and Kamath [18] with the aid of a 3D FEA. The stress intensity factor K varies along the leading edge of the crack, attaining a maximum very near the free surface. The ERR increases monotonically with crack length until steady-state conditions are reached where it remains unchanged thereafter at a value given by

$$G_{ss} = (\pi/2)\varepsilon^2 E_h h\, g(\alpha, \beta), \tag{4}$$

where E_h is the modulus of the hard Si layer and g a normalized ERR that depends on Dundur's material parameters α and β; Beuth [19] has calculated g with the aid of a 2D FEA for a wide range of α and β. Eq. (4) indicates that the steady-state crack length l_{ss} should scale with the product hg. The scaling factor may be found by considering the results of Ref. [18] for the case of a rigid substrate, i.e., $l_{ss} \approx 1.33$, $g = 0.71$, which leads to $l_{ss} = 1.8gh$.

The fracture behavior for a tunnel crack is similar to that discussed above except for changes in normalized ERR g due to changes in boundary conditions. For the present case the function g also depends on the nonlinear constitutive behavior of the interlayer, i.e.,

$$g = g(\alpha, \beta, \varepsilon/\varepsilon_{Yi}) \tag{5}$$

In determining the ERR we assumed $l > l_{ss}$ so that steady-state conditions prevail at the outset. Moreover, due to the collaborative nature of the cracking only the repeat portion of the structure shown in the upper part of Fig. 7a was considered, where dash-dot lines represent planes of mirror symmetry on the midplane of each layer. The ERR was determined with the aid of the FEM code according to $G = 2\Delta U/bh$, where ΔU is the energy released from the system following the

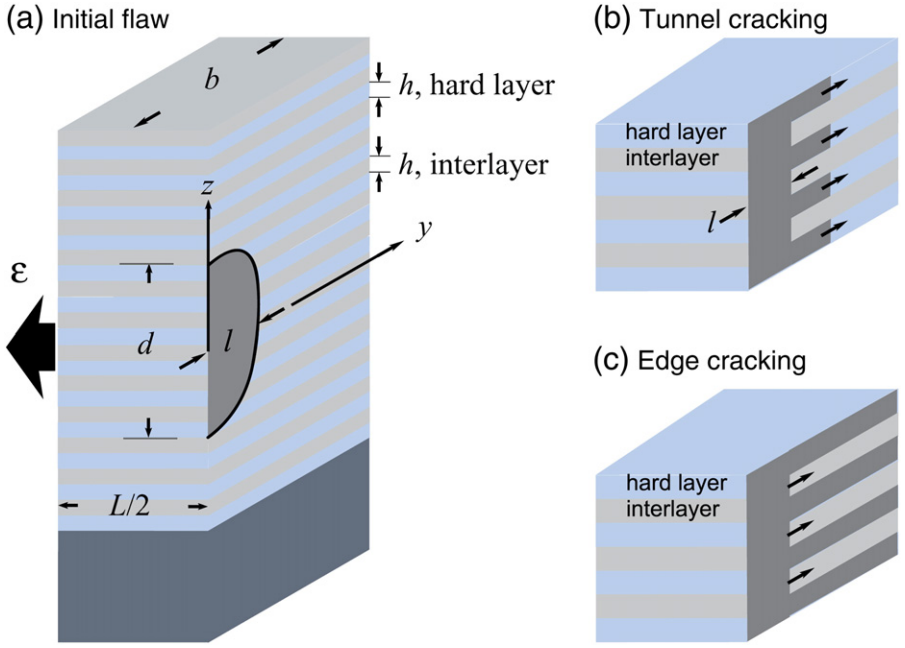

Fig. 6. Models used to predict onset of transverse cracking in a hard/soft multilayer due to tensile strain ε applied in the horizontal direction. Shown is a section through the plane of the initial flaw, with the darkest shade in the film indicating cracked areas. (a) An assumed initial edge flaw of dimensions d and l; (b) collaborative *tunnel cracking* in the hard layers; (c) *edge cracking* in the ductile interlayer.

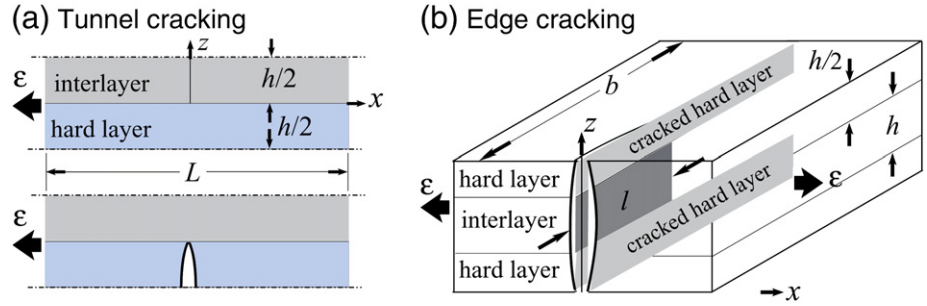

Fig. 7. Geometry of specimens used in the FEA for calculating normalized ERR. (a) Collaborative tunnel cracking in the hard layers (Fig. 6b); (b) edge cracking in the interlayers (Fig. 6c). The tensile strain is applied in the horizontal direction. The dash-dot lines in panel (a) indicate planes of mirror symmetry along the midplanes of the layers.

introduction of a crack into the horizontally strained hard layer, see the lower part of Fig. 7a. The half-specimen length $L/2$ was taken to be 100 times the layer thickness h, which was found to produce results insensitive to the specimen boundaries. The FEM grid near the crack tip was refined until convergence was achieved. With the ERR so determined, the function g can be found from Eq. (4). Fig. 8 (open symbols) plots the variation of g with normalized strain $\varepsilon/\varepsilon_{Yi}$. The plasticity of the interlayer manifests itself in the rather minor increase of g with increasing applied strain [20]. Assuming that the yield strain in the nanometer thickness range for our interlayer is on the order of 4% [16], the largest crack initiation strain in this study (i.e. $\approx 1.5\%$, see Fig. 5) corresponds to $\varepsilon/\varepsilon_{Yi} \approx 0.4$ in Fig. 8. Within this range the function g is nearly a constant.

4.2. Edge cracking (Fig. 6c)

The configuration in this case is that of an edge crack of length l in an interlayer of thickness h that is constrained by cracked hard layers above and below, see Fig. 7b. This poses a formidable 3D fracture problem. Here we simply treat that problem as a 2D edge crack in a linearly elastic homogeneous medium with effective modulus $E_{ef} = (E_h + E_i)/2$, for which the ERR is given as

$$G_e = 1.25\pi\varepsilon^2 E_{ef} l \tag{6}$$

4.3. Analysis of fracture events

At issue is which one of the two fracture modes discussed above controls the fracture. The controlling mode must exhibit the strain vs. layer thickness trend $\varepsilon_i \sim h^{-1/2}$ observed experimentally (Fig. 5). Consider first the crack tunneling mode (Fig. 6b). Because the normalized ERR g is nearly independent of the applied strain (Fig. 8), with a material-dependent critical value $G_{ss} = G_{Ch}$, where G_{Ch} is the fracture energy of the Si layer, the observed trend is readily obtained from Eq. (4). For the tunnel cracking analysis to apply the initial flaw dimension l must exceed $l_{ss} = 1.8gh$ or, with g taken as 0.82, $l/h > 1.5$, i.e., a flaw only slightly larger than one layer. On the other hand the edge cracking mode (Fig. 6c) depends on the initial flaw size and hence it may not be the controlling fracture mode. In order for edge cracking to follow channel cracking without any addition of load as required one must have $G_e/G_{ss} > G_{Ci}/G_{Ch}$, where G_{Ci} is the fracture energy of the (Ag) interlayer. Using Eqs. (4) and (6), this leads to

$$l/h \;>\; 0.4\, g(E_h/E_{ef})G_{Ci}/G_{Ch} \tag{7}$$

To get a sense of the dimensions involved consider a fracture energy ratio $G_{Ci}/G_{Ch} = 10$. Inserting this in Eq. (7) together with material data from Table 1 while taking for simplicity the normalized ERR g as 0.82 gives $l/h > 4.4$. Sufficient flaws exceeding this critical size are evidently found in these materials, not unreasonable considering the initial surface finish of the substrates. Accordingly, tunnel cracking in the hard layer shown schematically in Fig. 6b with the ERR given by Eq. (4) is proposed to be the controlling fracture mode. With G_{ss} taken as G_{Ch}, the crack initiation strain for the system is given by

$$\varepsilon_i = (2G_{Ch}/\pi g E_h h)^{1/2}, \tag{8}$$

where g (for the present system) is given in Fig. 8. This prediction is shown as a solid line in Fig. 5, where for simplicity we use a fixed value for normalized ERR g, i.e. 0.82, and $G_{Ch} = 0.06$ N/m (or fracture toughness $K_C = 0.09$ MPa m$^{1/2}$) giving a reasonable fit.

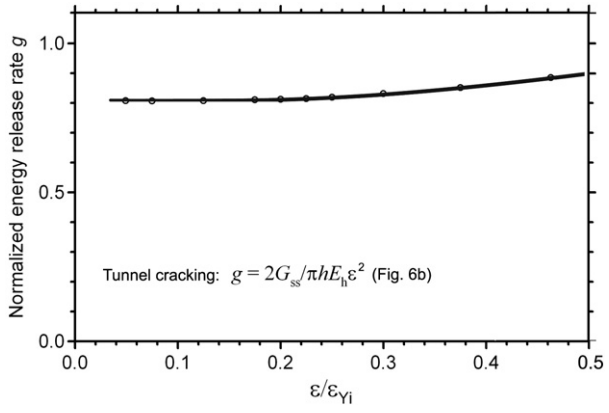

Fig. 8. FEM predictions (symbols, fitted by curve) of normalized ERR for tunnel cracking (Fig. 6b) as function of normalized tensile strain in a multilayer composed of equal-thickness brittle Si layers and elastic-perfectly plastic interlayers.

5. Discussions

The increase in crack initiation strain ε_i with decreasing layer thickness h found for our Si/Ag multilayers points to the advantage of using nanoscale material architecture for reasons of fracture. In addition to its dependence on h, Eq. (8) shows that ε_i also increases with increasing toughness of the layer and decreasing Young's modulus of the hard layer. For an applied strain not exceeding much the yield strain of the interlayer the post-yield behavior of the interlayer generally has only little effect on the normalized ERR g (Fig. 8). In such cases the latter can fairly accurately be obtained from the linear-elastic analysis of Beuth [19]. To realize the strength benefit noted above, the interlayer must be compliant and tough so as to force tunnel cracking in the hard layers. Although the thicknesses of the hard and soft layers used in this study are identical, use of relatively thin interlayers would still be effective as confirmed by tensile tests on Ni/Cu multilayers with a Cu to Ni thickness ratio as little as 0.1 [4] or by indentation tests on glass/epoxy multilayers, where it is shown that interlayers as thin as 1 μm are capable of confining the tunnel cracks to the hard layers [21]. Indeed, this is a basic design concept in

biological structures where the thickness ratio between the ductile organic layers and the brittle mineral layers is a tiny fraction of unity [22–24].

Finally we consider the fracture energy of nanoscale layers. Fracture tests using film/substrate bending configurations with 43 to 420 nm thick SiO_x films [25], 50 to 400 nm thick SiN_x films [26] and 5 to 125 nm thick Al_2O_3 films [10] show little, if any, thickness effect on fracture energy. Such results tend to justify our use of a fixed toughness value for the hard Si layers when constructing the solid line in Fig. 5. Our fracture energy value for pure Si (0.06 N/m) is well below those for SiO_x ($G_C \approx 10$ N/m [25]) and SiN_x ($G_C \approx 5$ N/m [26]). This difference likely reflects the toughening effect provided by the O_x and N_x constituents. The case of ductile films is more complex, and we are unaware of published works that take into consideration the inelastic response of the film material when calculating fracture energy. Eq. (8) may be used to extract this quantity in multilayer films similar to the present Si/Ag system. For example, Ref. [9] studied crack fragmentation in multilayers consisting of 20 layers of Cu and Ni, each of thickness 50 nm, that were sputter-deposited on a polyimide substrate. Assuming Ni to be the brittle phase in our analysis and using reported material values $E_i = 120$ GPa, $\nu_i = 0.34$, $E_h = 208$ GPa and $\nu_h = 0.32$, we obtain a normalized ERR $g = 1.17$. Using this in Eq. (8) together with the reported crack initiation strain $\varepsilon_i = 0.3\%$ leads to $G_C = 0.17$ N/m for Ni. This differs substantially from the reported value of 25 N/m obtained from the tunnel crack relation in Eq. (4), which was obtained by considering the multilayer as a homogeneous film [9]. While we are unaware of an independent measurement for the fracture energy of nickel in the nanoscale thickness regime, we note that our predicted value (0.17 N/m) is in the ballpark of the present value for Si (0.06 N/m).

6. Summary and conclusions

The evolution of damage in a model brittle/ductile Si/Ag multilayer evaporated on polycarbonate, aluminum alloy or hard steel substrates was followed in real-time using a four-point bending specimen. The fracture was characterized by through-thickness transverse cracks that initiated from flaws on the edge or surface of the samples and proliferated with load. Over the 2.5 to 30 nm range of layer thickness studied, the crack initiation strain was insensitive to total film thickness and substrate material while increasing with decreasing individual layer thickness h, to a good approximation proportionally to $h^{-1/2}$.

A 2D FEA that takes into account the internal film architecture and the inelastic response of the Ag interlayer was developed to predict the effect of system variables on the strain needed to initiate a transverse crack. A fracture scenario consisting of tunnel cracking in the brittle Si layers that is immediately followed by edge cracking in the ductile Ag layers is shown to be consistent with the experimental results. The analysis quantifies the benefit of using nanoscale layering for improving fracture resistance of ultra-thin films. The main requirement on material selection is that the interlayers must be sufficiently compliant and tough in order to initially contain the tunnel cracks in the brittle layers. Finally, the explicit relation for the crack initiation strain obtained from the analysis offers means for obtaining fracture energy and designing against premature failure in nanoscale layered structures.

References

[1] S.L. Lehoczky, J. Appl. Phys. 49 (1978) 5479.
[2] D. Josell, D. van Heerden, D. Read, J. Bonevich, D. Shechtman, J. Mater. Res. 13 (1998) 2902.
[3] H. Huang, F. Spaepen, Acta Mater. 48 (2000) 3261.
[4] D. Tench, J. White, Metal. Trans. A 15 (1994) 2039.
[5] A. Duck, N. Gamer, W. Gesatzke, M. Griepentrog, W. Osterle, M. Sahre, I. Urban, Surf. Coat. Technol. 142–144 (2001) 579.
[6] D.R. McKenzie, R.N. Tarrant, M.M.M. Bilek, T. Ha, J. Zou, W.E. McBride, D.J.H. Cockayne, N. Fujisawa, M.V. Swain, N.L. James, J.C. Woodard, D.G. McCulloch, Diamond Relat Mater. 12 (2003) 178.
[7] A. Karimi, Y. Wang, T. Cselle, M. Morstein, Thin Solid Films 420–421 (2002) 275.
[8] E. Martınez, J. Romero, A. Lousa, J. Esteve, J. Appl. Phys. A 77 (2003) 419.
[9] X.F. Zhu, B. Zhang, J. Gao, G.P. Zhang, Scr Mater. 60 (2009) 178.
[10] D.C. Miller, R.R. Foster, Y. Zhang, S.-H. Jen, J.A. Bertrand, Z. Lu, D. Seghete, J.L. O'Patchen, R. Yang, Y.-C. Lee, S.M. George, M.L. Dunn, J. Appl. Phys. 105 (2009) 093527.
[11] N.S. Brar, C.H.M. Simha, J. Phys. IV 10 (2000) 611.
[12] M.A. Meyers, Dynamic Behavior of Materials, Wiley, New-York, NY, 1994.
[13] B.E. Alaca, M.T.A. Saif, H. Sehitoglu, Acta Mater. 50 (2002) 1197.
[14] X. Deng, N. Chawla, K.K. Chawla, M. Koopman, J.P. Chu, Adv. Eng. Mater. 7 (2005) 1099.
[15] M.D. Thouless, E. Olsson, A. Gupta, Acta Mater. 40 (1992) 1287.
[16] N.A. Mara, D. Bhattacharyya, P. Dickerson, R.G. Hoagland, A. Misra, Appl. Phys. Lett. 92 (2008) 231901.
[17] S.M. Han, M.A. Phillips, W.D. Nix, Acta Mater. 57 (2009) 4473.
[18] T. Nakamura, S.M. Kamath, Mech. Mater. 13 (1992) 67.
[19] J.L. Beuth, Int. J. Solids Struct. 29 (1992) 1657.
[20] J.L. Beuth, N.W. Klingbeil, J. Mech. Phys. Solids 44 (1996) 1411.
[21] H. Chai, G. Ravichandran, Eng. Fract. Mech. 76 (2009) 2526.
[22] S. Kamat, X. Su, R. Ballarini, A.H. Heuer, Nature 405 (2000) 1036.
[23] A. Woesz, J.C. Weaver, M. Kazanci, Y. Dauphin, J. Aizenberg, D.E. Morse, P. Fratzl, J. Mater. Res. 21 (2006) 2068.
[24] F. Barthelat, H. Tang, P.D. Zavattieri, C.-M. Li, H.D. Espinosa, J. Mech. Phys. Solids 55 (2007) 306.
[25] C.H. Hsueh, M. Yanaka, J. Mater. Sci. 38 (2003) 1809.
[26] J. Andersons, J. Modniks, Y. Leterrier, G. Tornare, P. Dumont, J.-A.E. Manson, Theor. Appl. Fract. Mech. 49 (2008) 151.